Zeolite-encapsulated single-atom catalysts for efficient CO_2 conversion

Gerard Alonso[†,§], Estefanía López[†], Fermín Huarte-Larrañaga[†], Ramón Sayós[†], Hector Prats[‡,*] and Pablo Gamallo[†,*]

[†] *Universitat de Barcelona and Institut de Química Teòrica i Computacional (IQTC), C / Martí i Franquès 1, 08028, Barcelona, Spain.*

[§] *Departamento de Ingeniería Química, Universidad de Concepción, C / Edmundo Larenas 219, 4030000, Concepción, Chile.*

[‡] *Department of Chemical Engineering, University College London, Roberts Building, Torrington Place, London WC1E 7JE, UK.*

* Corresponding authors: h.garcia@ucl.ac.uk, gamallo@ub.edu.

ABSTRACT: Zeolite-supported single-atom catalysts (SACs) have emerged as a novel class of cheap and tuneable catalysts that can exhibit high activity, selectivity and stability. In this work, we conduct an extensive screening by means of density functional theory calculations to determine the usefulness of 3d, 4d and 5d transition metal (TM) SACs-supported in MFI-type Silicalite-1 zeolite for CO_2 conversion. Two reaction mechanisms are considered, namely the redox −direct CO_2 dissociation− and associative −hydrogen-assisted CO_2 dissociation− mechanisms. Early TM SACs exhibit the lowest energy barriers, which follow the redox mechanism. These energy barriers raise when going right in the periodic table up to group 10, where they become prohibitive and the associative mechanism should dominate. By also considering their resistance to aggregation, we support the use of Sc, Y, La, Ru, Rh, Ni, Pd and Pt as potentially active and stable catalysts for CO_2 conversion, given their low energy barriers and strong interaction with the zeolite framework.

KEYWORDS: *Single-atom catalysts, Zeolites, MFI, Heterogeneous catalysis, CO_2 conversion, Transition metals, Density functional theory.*

Revision submitted to Journal of CO_2 Utilization (September 27th 2021)

1. Introduction

Proper control of atmospheric CO_2 content to fight climate change is one of the central challenges of mankind. Anthropogenic CO_2 is mainly produced via combustion of fossil fuels and is currently producing a notable environmental impact, such as in global warming [1]. Fortunately, CO_2 can be captured and transformed into other valuable chemicals (*e.g.,* formaldehyde, methane, methanol or bicarbonate, among others [2,3,4,5,6]) with the help of transition metal (TM)-based catalysts [7], mainly through Au, Pd, Cu, Ru, Ni, Pt, Pd, Rh or Fe [8,9,10,11,12,13,14]. However, since some of those TMs are expensive and scarce, it is still imperative to develop better catalysts to increase the efficiency and reduce the cost of the CO_2 conversion.

In the last few years, single-atom catalysts (SACs) finely dispersed into different supports have emerged as new promising materials for catalysis [15,16]. SACs aim to combine the large activity and selectivity of homogeneous catalysts but with the separation and reutilization capabilities of a heterogeneous catalyst [17,18]. Supported SACs have a higher activity/mass relationship due to a better metal utilization than nanoparticles, which makes them also more cost-efficient for catalysis. Some of the early successful reactions were carried out in oxide and graphene supported SACs including CO oxidation [19], water-gas shift reaction [20,21], hydroformylation of olefins [22] and methanol and benzene oxidations [23,24]. The great activity of SACs is correlated to their low coordination numbers, which means they can be partially deactivated if they diffuse through the support and aggregate forming nanoparticles. For this reason, it is not only important to find a good SAC for a given application, but it is also critical to disperse it into a support that can stabilize it (*i.e.,* prevent the metal atoms from clustering). In that sense, many efforts are devoted to preventing SAC surface migration by depositing the TM in surface vacancies [25,26,27,28], or spatially confining them in microporous materials (*e.g.,* zeolites or metal-organic frameworks) [29,30,31,32].

From all those promising supports, we have turned our attention to zeolites [33], where important successes were achieved in the last years by encapsulating different TM atoms in structures with different Si/Al ratio to carry out CO oxidation [34], methane conversion to higher hydrocarbons [35], to methanol and to acetic acid [36] or n-hexane isomerization [37], among others [16]. Pd SACs were also anchored to mesoporous silica SBA-15 [38] and used to hydrogenate alkynes. Finally, Ru and Rh SACs were recently encapsulated in the fully silicated MFI structure (*i.e.,* TM_1@Silicalite-1 or simply TM_1@S-1) [39,40] and the resulting catalysts were promising for H_2 production from ammonia borane hydrolysis and ammonia synthesis, respectively. The encapsulation of metal atoms in zeolites requires a strict control of experimental conditions, since high pH and/or temperature might lead to particle aggregation [41]. Available synthesis techniques include direct synthesis from inorganic or ligand-assisted metal precursors, multistep post-synthesis encapsulation (*e.g.,* two-step dry-gel-conversion) or ion-exchange followed by reduction, as described by Chai *et al.,* [42]. From the very large number of potential SAC+support combinations, only less than 10 TMs have actually been synthesized as SACs. Such a small number evidences the need of a systematic screening for catalysts with large activity whilst still being stable at operative conditions. In a previous study [43], we computationally assessed the structure and stability of all period IV-VI TM_1@S-1 (except for Tc due to its radioactive nature), showing that TMs can be encapsulated via dispersion + electrostatic interactions in the MFI framework, which can be quite strong since the adsorption energies range from -0.48 eV (for Cu and Zn) to -1.67 eV (for Pt).

Herein, we evaluate the potential activity of this set of SACs for CO_2 conversion. Due to the large number of systems included in this screening study and the large amount of possible reaction products, it was not feasible to build the full reaction profiles for each SAC. Instead, we focus on the first steps of CO_2 activation, which involve the adsorption of reactants (CO_2 and H_2), direct CO_2 dissociation through the redox mechanism ($CO_2 \rightarrow CO + O$), H_2 dissociation ($H_2 \rightarrow H + H$) and hydrogen-assisted CO_2 dissociation through the associative mechanism, either via formate ($CO_2 + H \rightarrow HCOO$) or carboxylate ($CO_2 + H \rightarrow COOH$) intermediates.

Note that the experimental viability of TM_1@S-1 synthesis was already proven for Rh_1@S-1 and Ru_1@S-1 [39,40], so the results from this study will serve to assess how adequate are those catalysts in comparison to other non-synthesized TM_1@S-1 and for proposing novel catalysts capable of adsorbing and converting CO_2. The results obtained here will provide a solid theoretical background from which potential catalytic activity can be predicted, paving the road for further experimental and computational studies on this topic.

2. Computational details

The MFI Silicalite-1 has a microporous $Si_{96}O_{192}$ unit cell composed by SiO_4 tetrahedra (T) units positioned at 12 non-equivalent T sites (*i.e.,* T1-T12). The framework O atoms are located at 26 distinct O sites (*i.e.,* O1−O26). This arrangement leads to a 3D pore system with straight ten-membered-ring (10-MR) channels in the [010] direction intersected by sinusoidal 10-MR channels in the [100] direction, as shown in Fig. 1. The most stable structures of each one of the 29 TM_1@S-1 SACs were taken from our previous study [43]. In summary, we employed Density Functional Theory (DFT) calculations to find the most stable site to adsorb each TM in the pristine S-1 structure by optimizing the geometry of each TM placed in all possible non-equivalent positions of all pores. With this procedure, we located only 6 preferred sites in S-1 by the entire set of TM adatoms. Most TM atoms adsorb via van der Waals (vdW) interactions into the sinusoidal 10-MR channels at distances larger than 2.7 Å. Among all possible positions in these channels, only 3 specific adsorption sites are preferred by the TM atoms, which are denoted as Channel X (X = A, B or C) sites (see Fig. 1). The only exceptions are group 3 TMs (*i.e.,* Sc, Y and La), which prefer to adsorb in the middle of the quadrilaterals formed by two O16 and two O25 atoms (*i.e.,* O16(×2)−O25(×2) site); Group 10 TMs (*i.e.,* Ni, Pd and Pt) and Ru atoms, which are found closely coordinated with O18 and O23 atoms (*i.e.,* O18−O23 site) and weakly coordinated to O16(×2); and finally, Rh atoms, which are located in the middle of the quadrilaterals formed by O8, O11, O18 and O26 atoms (*i.e.,* O8−O11−O18−O26 site). In all those systems the porous support provides protection against SAC sintering via 3D confinement, except in group 3 TMs where the S-1 also accepts part of their electron density changing their electronic structure. Notice that, Ru and Rh are the only TMs experimentally encapsulated in Silicalite-1, and their coordination according to EXAFS fittings agree with our DFT-based predictions, both suggesting TM coordination with four O atoms. However, DFT results slightly overestimates the average Ru−O distance (r(DFT) = 2.15 Å) by a 7% [40] and the Rh−O distance (r(DFT) = 2.40 Å) by a 18% [39] with differences in TM-O bonds lower than 0.01 Å between DFT and DFT-D3 geometries. For a more complete description of those sites, the reader is referred to the original work [43]. Additionally, images of each TM location are compiled in Fig. 1.

Fig. 1. Position of the preferred adsorption sites for all TM atoms encapsulated in zeolite S-1 according to Ref. [43]. TMs in Channel A/B/C interact weakly with the S-1 structure, whereas the other three sites bind closely to O rings of the pore walls. SiO_4 units are represented by blue tetrahedra with Al and O atoms shown in yellow and red spheres, respectively. The a, b and c unit cell directions correspond to the red, green and blue arrows, respectively.

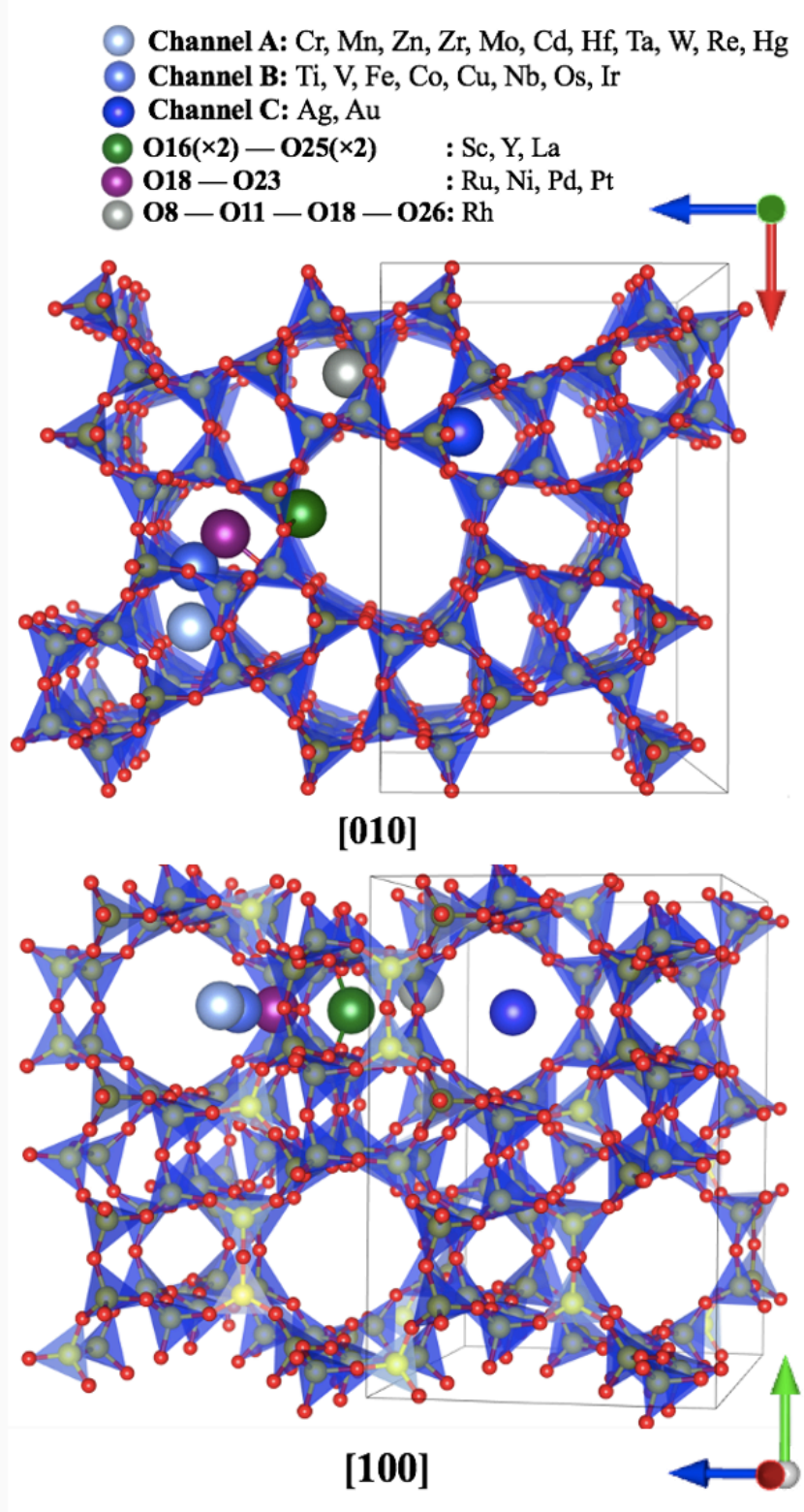

To be consistent with our previous study [43], the Vienna Ab Initio Simulation Package (VASP) [44] was used to perform all periodic DFT calculations by employing the Perdew-Burke-Ernzerhof [45] exchange-correlation functional, plus the Grimme D3 dispersion correction (PBE-D3) [46]. The valence electron density was expanded in a 600 eV kinetic energy plane-wave basis set, which gave total energy variations below 0.01 eV. The effect of core electrons on the valence electron density was accounted through the Projected Augmented Wave (PAW) method [47], as implemented in VASP by Kresse and Joubert [48]. Spin-polarization was taken into consideration to reflect the TM_1@S-1 magnetic properties. Due to the large size of the simulation cells (*i.e.,* around 290 atoms with a = 20.09 Å, b = 19.74 Å and c = 13.37 Å), only the Γ-point was used to sample the Brillouin zone.

The most stable site for the adsorbed species was obtained by screening several initial geometries with different positions and orientations. The tolerance for the conjugate gradient algorithm to minimize energy and forces on atoms was set to 10^{-5} eV and 0.01eV/Å, respectively. Adsorption energies ($\Delta E_{ads,i}$) were calculated as:

$$\Delta E_{ads,i} = E_{i-SAC} - E_{SAC} - E_{i(g)} \quad (1)$$

where E_{i-SAC} is the total energy of adsorbed i species in the TM_1@S-1 SAC, E_{SAC} is the energy of the clean SAC (*i.e.,* the relaxed pristine TM_1@S-1 structure) and $E_{i(g)}$ is the energy of species i in gas-phase and in its ground electronic state. With this definition, negative values of $\Delta E_{ads,i}$ indicate favorable adsorption. The latter term was calculated in a simulation cell with the same parameters than the TM_1@S-1 using only the Γ-point. The energy barriers ($\Delta E^{\neq}$) and reaction energies (ΔE_r) were calculated as:

$$\Delta E^{\neq} = E_{TS-SAC} - E_{R-SAC} \quad (2)$$

$$\Delta E_r = E_{P-SAC} - E_{R-SAC} \quad (3)$$

where E_{TS-SAC} is the energy of the transition state (TS), E_{R-SAC} is the energy of the initial configuration (*i.e.,* adsorbed reactants), and E_{P-SAC} the energy of final configuration (*i.e.,* adsorbed products). All TSs were located by using the Climbing-Image Nudged Elastic Band (CI-NEB) method [49]. The initial guesses for the employed intermediate images were created through the Image Dependent Pair Potential (IDPP) interpolation procedure [50] as implemented in the Atomic Simulation Environment (ASE) [51]. All adsorption minima and TSs were characterized through frequency calculations by computing the elements of the Hessian matrix as finite differences of 0.03 Å length and considering only displacements of the adsorbate. Note that the Zero Point Energy (*ZPE*) term is included in all reported energy values unless otherwise indicated. Additionally, the Gibbs free energy of adsorption, reaction and free energy barriers were calculated by correcting the respective E values in Eq. 1-3 with the corresponding temperature/pressure correction to the free energy. For gas-phase species, the correction was obtained using the ideal gas approximation, whereas for adsorbed species the harmonic oscillator model was used for all degrees of freedom [52].

Finally, to further understand the interaction between metal atoms, reactant molecules and the support, we computed the atomic charges on the supported transition metal atoms (Q_{TM}), the total net charges on the zeolite (Q_{Zeo}) and on the adsorbed CO_2 and H_2 species (Q_{CO_2} and Q_{H_2}) through a Bader analysis of the electron density [53].

3. Results and discussion

3.1. Interaction of the metal atoms with CO_2 and H_2

Prior to CO_2 conversion by either the redox or associative mechanisms, CO_2 and H_2 species must adsorb on the SAC and, for H_2, it must also dissociate to give rise to adsorbed H species that are required in the associative pathway. In this section, we study the molecular adsorption of CO_2 and the adsorption and subsequent dissociation of H_2 species, evaluate their geometry and their electronic structure.

CO_2 physisorbs on the pristine S-1 structure mainly by vdW interactions, leading to a weak $\Delta E_{ads,CO_2}$ (see Figs. 2a-d and Table S1 in the SI). However, the presence of single TM atoms in general leads to a stronger chemisorption of CO_2, which typically interacts with the metal atom through the C−O bond (*i.e.,* η(CO) configuration in Fig. 3) with an average C−TM distance of around 2 Å. During this adsorption step, the C−O bond is elongated from the gas-phase value of 1.18 Å to 1.22−1.46 Å and the O−C−O angle is bent from 180º to 120−150º. This activated configuration leads to a significantly strong adsorption energy (*i.e.,* $\Delta E_{ads,CO_2} \lesssim -1$ eV). In general, the binding strength of CO_2 on the supported TMs decreases along a period and moving up along a group (Fig. 2a), with a limit on group 11 and 12 TMs, where it weakly physisorbs with no noticeable perturbation from its gas-phase geometry. Other exceptions are those TMs with semi-occupancy of *d* orbitals (*i.e.,* Mn and Re with s^2d^5) and group 4 TMs, where CO_2 does not have a stable configuration (*i.e.,* Hf) or where it binds in a η(O) configuration instead of η(CO) (*i.e.,* Ti and Zr). Notice that, for Hf, $\Delta E_{ads,CO_2}$ is calculated by considering CO + O as the adsorbed state.

Fig. 2. CO_2 and H_2 (a,g) adsorption energies ($\Delta E_{ads,i}$), (b,h) Bader charges for TM (Q_{TM}), the S-1 zeolite (Q_{Zeo}) and the net Bader charges of adsorbed species (Q_{CO_2}, Q_{H_2}), (c) C−O bond distances, (i) H−H bond distances, (d) O−C−O angle bendings, (e,j) dissociation energies (ΔE_r) and (f,k) dissociation energy barriers ($\Delta E^{\neq}$) in the full set of TM_1@S-1 SACs. Energy barriers are compared with some other popular catalysts for C−O and H−H cleavage. In all plots red, blue and green correspond to TMs from period IV, V and VI, respectively. Stars correspond to spontaneous dissociative adsorptions, where only $\Delta E_{ads,i} = E_{P-SAC} - E_{SAC} - E_{i(g)}$ and $\Delta E^{\neq} = 0$ is shown. Numerical values used are shown in Tables S1 and S2 in the SI.

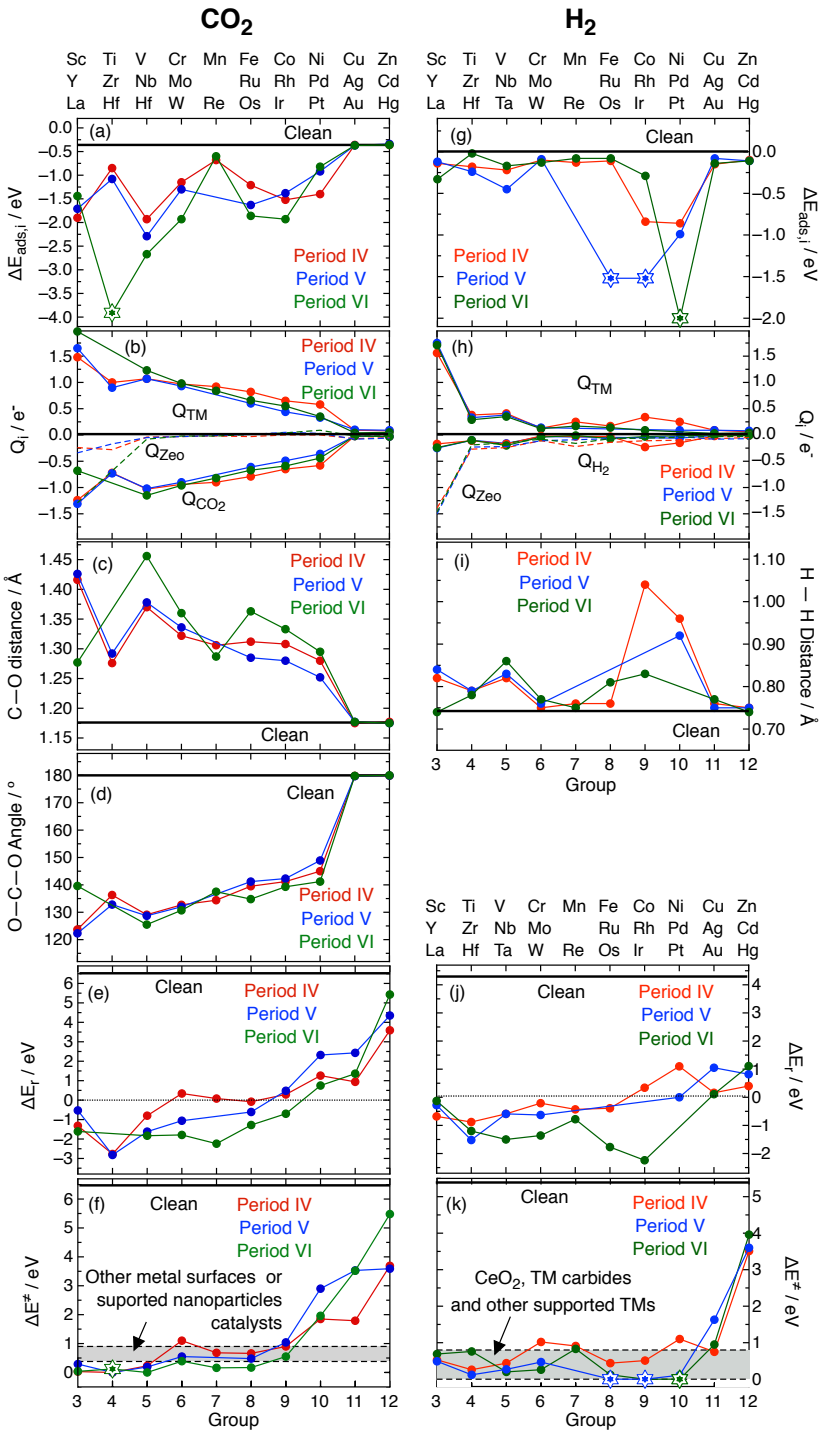

During the adsorption process, there is a significant TM-to-CO_2 charge transfer, which is evidenced by the final oxidation state of the metal atom (*i.e.,* $Q_{TM} > 0$) and the negative net charge on CO_2, as shown in Fig. 2b. The atomic Bader charges on the TM atoms decrease along a period, which in part can be rationalized due to the higher electronegativity of the metal atom. On group 11 and 12 TMs, the charge transfer is negligible, due to the weak CO_2 – TM physisorbed interaction, and therefore the net charges on the TM and CO_2 are almost zero. Despite the fact that in most cases there is only charge transfer between the TM atom and CO_2 (*i.e.,* $Q_{TM} + Q_{CO_2} \approx 0$), in the case of group 3 TMs, there is also a significant TM-to-zeolite charge transfer evidenced by the negative net Bader charge on the zeolite. This charge transfer occurs due to the very strong interaction between group 3 TM atoms and the zeolite support, as discussed in our previous work [43]. When this occurs, part of the charge density still remains in the zeolite after CO_2 adsorption. Interestingly, stronger adsorption energies are correlated with longer C−O bond lengths, while more negative Q_{CO_2} are correlated with longer C−O bond lengths and lower O−C−O angles (see Fig. S1 in the SI).

H_2 also physisorbs into the pristine S-1 via vdW interactions leading to a weak $\Delta E_{ads,H_2}$ (see Figs. 2g-i and Table S2 in the SI). In the presence of TMs from groups 3, 4, 5, 9 and 10, as well as for Os, H_2 chemisorbs with $\Delta E_{ads,H_2}$ values up to −0.99 eV and in a η(HH) configuration, as illustrated in Fig. 3. In those TMs, the equilibrium H−TM distance lays between 1.5 Å and 2.5 Å and the H−H bond is elongated from 0.75 Å (gas-phase) up to 1.00 Å. Within this sub-set, the H_2 binding strength increases when moving right along a period and down in a group. Additionally, H_2 breaks spontaneously (with no energy barrier) in Ru, Rh and Pt. In these cases, $\Delta E_{ads,H_2}$ values are calculated by considering H + H as the adsorbed state. In the remaining TMs (*i.e.,* groups 5, 6, 7, 8, 11 and 12, except Os and Ru), H_2 weakly physisorbs and no relevant change with respect the gas-phase geometry or charge transfer is observed. Noticeably, $\Delta E_{ads,H_2}$ and Q_{H_2} are correlated with the H−H distance in the adsorbed state, as shown in Fig. S2 in the SI.

Fig. 3. Characteristic reaction pathways for direct CO_2 dissociation, H_2 dissociation and H-assisted CO_2 dissociation. Optimized geometries for the initial, transition and final states are shown in the left, middle and right panels, respectively. SiO_4, units are represented by blue tetrahedra with yellow Si and red O atoms. TM atoms are shown either as cyan or purple spheres (consistent with the site colour coding presented in Fig. 1) and C, O and H are shown as brown, red and white spheres, respectively. All panels corresponding to the same reaction path share the same orientation, as shown by the lower-right hand axis where red, green and blue arrows represent the a, b and c directions, respectively.

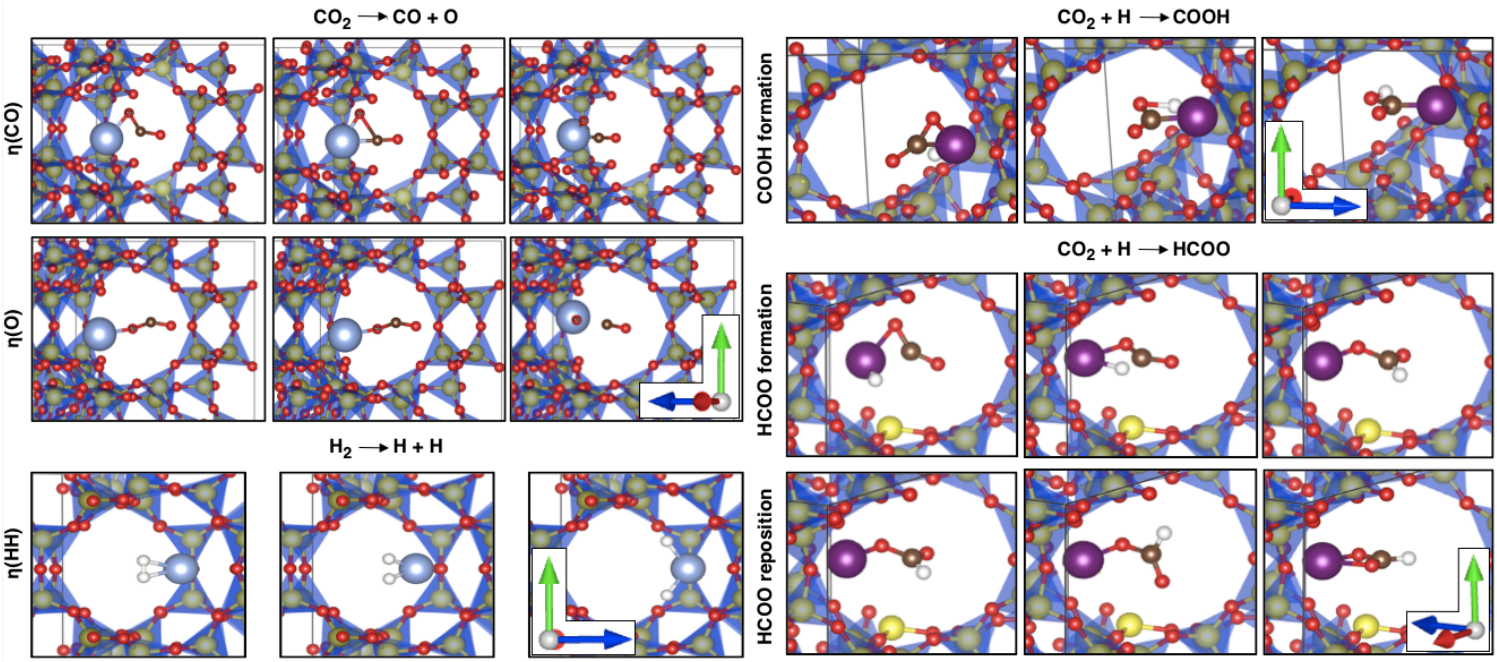

The reaction energies and energy barriers for H_2 dissociation are compiled in Figs. 2j-k and in Table S2 in the SI. The pristine S-1 framework does not dissociate H_2, since the weak binding with the framework atoms results in a gas-phase-like highly endoergic reaction with a prohibitive energy barrier larger than 5 eV. However, H_2 dissociates in almost all considered SACs with low energy barriers, being barrierless for Ru, Rh and Pt, as mentioned above. Interestingly, H_2 dissociation is exoergic in almost all group 3-9 TM SACs, with ΔE_r up to -2.20 eV and $\Delta E^{\neq} \leq 1.02$ eV. Those barriers are comparable to other good H_2 dissociation catalysts such as CeO_2 [54], TM_1/CeO_2 [55], $(Ni_2, Cu_2)/MgO$ [56] or TM carbides [57], which show $\Delta E^{\neq}$ values from almost zero to 0.8 eV. On the other hand, in TMs from groups 11 and 12 the reaction becomes endoergic and $\Delta E^{\neq}$ increases significantly, with prohibitive values for group 12 SACs. The most common dissociation pathway for TMs where H_2 adsorbs in η(HH) configuration involves further H−H bond elongation, yielding to the coadsorbed H + H on the TM atom. Otherwise, when H_2 only physisorbs around 3 Å from the TM, it first needs to get closer to the metal, relocate as η(HH) and then, break.

It is worth noting that for TM SACs adsorbed very close to the S-1 zeolite wall (*i.e.,* group 3, group 10, Ru and Rh SACs) the CO_2 adsorption typically promotes a small surface reconstruction, where the TM + CO_2 pair separates slightly from the zeolite wall to reduce the repulsive CO_2−zeolite interactions. Similarly, the H_2 adsorption only promotes a small surface reconstruction on top of Ni and Pd TM SACs due to the H_2 smaller size and weaker H_2−zeolite repulsion. However,

the cleavage to H + H leads to an equivalent reconstruction of group 3, Rh and Pt TMs. For a more precise picture of the surface reconstruction the reader is referred to Section S4 of the SI, where the original TM_1@S-1 structure and the deformation caused by CO_2/H_2 is compiled for the full set of TMs. Also, all geometry files for each stationary point characterized in this work have been uploaded to a public repository (See Appendix A).

3.2. Redox mechanism

The redox mechanism involves the C−O bond breaking by direct CO_2 dissociation to CO + O. The calculated reaction energies and energy barriers for this step are compiled in Fig. 2e-f and Table S1 in the SI. For the un-aided CO_2 dissociation in the pristine S-1 with no TM, the weak interactions among the support, the reactants and the products lead to a gas-phase-like highly endoergic reaction with a prohibitive energy barrier ($\Delta E^{\neq} > 6$ eV). However, the presence of single TM atoms stabilizes the reaction products, yielding to affordable reaction barriers and even barrierless dissociations in a few cases.

ΔE_r and $\Delta E^{\neq}$ follow a similar trend than the $\Delta E_{ads,CO_2}$ along the periodic table, meaning that the reaction is more favourable in TM SACs from the bottom left of the periodic table and less favourable when moving right along a period and up along a group. As shown in Fig. 2e, the reaction is highly exoergic (*i.e.,* high negative values up to −2.8 eV) for early TMs, and proceeds with very low reaction barriers (*i.e.,* 11 TM_1@S-1 catalysts belonging to groups 3−8 break CO_2 with $\Delta E^{\neq} < 0.30$ eV, 5 of them with $\Delta E^{\neq} < 0.10$ eV). These values contrast with the typical $\Delta E^{\neq}$ ranging from 0.38 eV to 0.90 eV reported for other catalysts [58], such as flat metal surfaces [59,60,61] or supported metal clusters [62,63,64], placing many TM_1@S-1 from groups 3−8 as extremely active towards direct C−O bond cleavage. In those TMs, CO_2 is expected to be transformed via redox pathway, because it follows a single unimolecular step with a very low reaction energy barrier. In contrast, TM_1@S-1 of groups 10−12 are poor catalysts for the direct CO_2 dissociation, with prohibitive energy barriers due to their inability to stabilize the reaction products and their weak interaction with CO_2. This implies that hydrogen-assisted associative pathways could dominate in these cases.

As suggested by Pallasana and Neurock [65] and popularized by Nørskov *et al.,* [66] the correlation between reaction energies and energy barriers in heterogeneous catalysed reactions is expected to follow the Brønsted-Evans-Polanyi (BEP) [67,68] relationship. Specifically, the transition state energy (E_{TS}) and the dissociative reaction energy (E_r) defined by Wang et al. [69] as Eq. 4 and 5 (without ZPE) are used to compare with the universal BEP relation for extended TM surfaces.

$$E_{TS} = E_{TS-SAC} - E_{SAC} - E_{i_{(g)}} \quad (4)$$

$$E_r = E_{P-SAC} - E_{SAC} - E_{i_{(g)}} \quad (5)$$

Indeed, a quantitative BEP relationship for CO_2 dissociation on TM_1@S-1 emerges when plotting E_{TS} in front of E_r as shown in Fig. 4. The obtained scaling line has a similar slope than the universal BEP relation [69], but with E_{TS} values about 1 eV lower. This fact evidences that S-1 encapsulated TM SACs are much more active for C−O bond scission than their extended TM counterparts. Note that several TM_1@S-1 feature negative E_{TS} and E_r values, unachievable by extended metal surfaces, which only get as low as E_{TS} = 0.88 eV and E_r = −2.00 eV. Unfortunately, the activation of H_2 does not seem to follow a clear BEP relationship as shown in Fig. S3 in the SI.

Fig. 4. Comparison between the BEP relationship for C−O bond dissociation on TM_1@S-1 (blue line) and the universal BEP relationship reported by Wang et al. [69] for extended metal surfaces (black line). Group 4 TMs (green points) were excluded from the fit because the TS does not correspond to a pure C−O elongation.

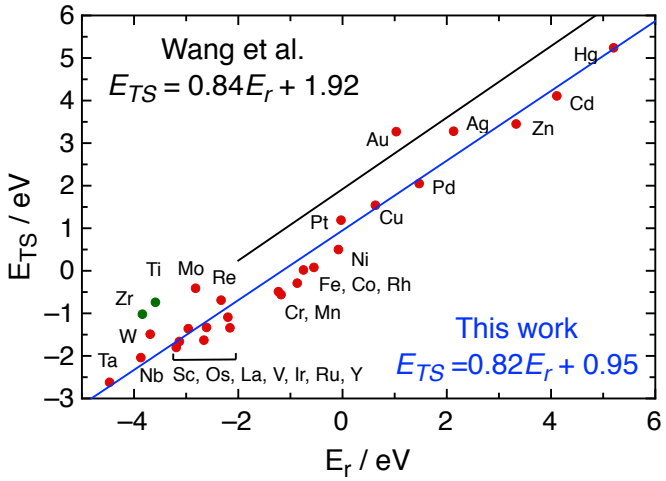

The most common dissociation pathway involves further C−O bond elongation of the adsorbed CO_2 in η(CO) configuration, yielding to the reaction products CO and O, coadsorbed on the TM atom. There are, however, a few alternative dissociation pathways followed by some TM_1@S-1, which we describe below. In the case of La_1@S-1, the CO_2 + La pair needs to slightly separate from the S-1 wall in order to have enough space to accommodate the products. During this translation, the CO_2 molecule dissociates in an apparently barrierless process, with the imaginary frequency of the located TS corresponding to the translation of the CO_2 + La pair moving away from the S-1 wall. For Ti and Zr, where CO_2 is adsorbed in η(O) configuration, it breaks with no energy barrier before reaching the η(CO) configuration, and the imaginary frequency of the TS corresponds to a rotation from the η(O) to the η(CO) configuration, which also includes an elongation of the C−O bond. On the other hand, Hf spontaneously breaks the CO_2 into CO + O. Next, for TMs of group 11, the reaction is highly endoergic, and the system must overcome a very large endothermicity to bring the CO_2 closer from its initial physisorbed state to a η(CO) configuration. Then, the C−O bond breaks and the O atom is first adsorbed onto the TM. Since the coadsorbed CO + O products are not stable, the adsorbed O species diffuses to the opposite side of the TM and then CO stays adsorbed through the C atom. Finally, for the case of group 12 TMs, the reaction is even more endoergic due to the low stability of the reaction products. The CO_2 dissociation proceeds through a direct gas-phase-like elongation of the C−O bond from its η(C) physisorbed state leading to adsorbed O and a weakly physisorbed CO in a η(C) configuration. Further information along with snapshots of the reaction pathway are found in Section S4 of the SI.

3.3. Associative mechanism

As mentioned above, many TMs exhibit extremely low reaction energy barriers to convert CO_2 through the redox pathway. Since the dissociation is an unimolecular step, it is not expected that bimolecular steps (such as hydrogenations in the associative pathway) will be kinetically relevant, even in the case of low energy barriers. For this reason, we have decided to consider this alternative pathway only in a subset of TM_1@S-1 in which the redox mechanism has a significant energy barrier. This includes the late TMs in group 10 (*i.e.,* Ni, Pd and Pt), where CO_2 adsorbs strongly but it is hard to break, and

also Ru and Rh, which have been already synthesized experimentally, proven to be highly active catalysts, and can dissociate H_2 spontaneously.

In those five TMs, CO_2 adsorbed as η(CO) can react with a coadsorbed H species by forming an O−H bond leading to the carboxyl intermediate (*i.e.,* COOH), which is bonded to the TM via the C atom (see Fig. 3). Alternatively, the H atom can react with the C atom forming a C−H bond leading to the formate intermediate (*i.e.,* HCOO), which is first produced in its monodentate configuration (m-HCOO), bonded to the metal through one of its O atoms. Then, m-HCOO rearranges itself leading to the lower energy bidentate configuration (b-HCOO), in which the formate is bonded to the metal through both its O atoms. The reaction energies and energy barriers for both pathways (plus the redox for comparison) are compiled in Fig. S4 and Table S3 in the SI. To compare those pathways in actual operative conditions, the Gibbs free energy diagrams at 600 K and 1 atm were built and shown in Fig. 5. To our knowledge, CO_2 conversion in TM_1@S-1 is currently not assessed experimentally, so those conditions were selected as they are generally used in similar systems [40,70] or other CO_2 conversion catalysts [71]. Finally, the geometry for each minimum and TS are shown in Section S4 of the SI.

The present results suggest that CO_2 conversion steps on group 10 TMs (*i.e.,* Ni, Pd and Pt) should follow the associative mechanism via COOH or HCOO intermediates, as the free energy barrier for their formation are much lower than for the direct CO_2 dissociation (Fig. 5). In the case of Ni, the HCOO pathway is much more favoured than the COOH pathway. However, after H_2 dissociation, the H + H recombination is barrierless, implying that the activity of the associative mechanism will be limited by the small amount of H species present in the catalyst. For Pd and Pt, the dissociation of H_2 is very favoured and there will be a strong competition between the HCOO and COOH pathways, as both exhibit similar free energy barriers. For this reason, kinetic modelling techniques such as kinetic Monte Carlo [61] or microkinetic modelling should be employed to truly identify which pathway is more dominant. However, developing an accurate model for the TM_1@S-1 catalysts requires further study due to their uncommon 3D morphology and is out of the scope for this work. Finally, we show that Rh and Ru would follow the redox mechanism, since, apart from being unimolecular, have lower free energy barriers compared to COOH or HCOO associative pathways.

Fig. 5. Gibbs free energy profiles for CO_2 conversion in Ni, Pd, Pt, Rh and Ru at standard operative conditions (*i.e.,* 600 K and 1 atm), with the zero of energy taken as $CO_{2(g)} + H_{2(g)} + TM_1$@S-1. The numerical values used in this figure are compiled in Table S3 in the SI. Note that the free energy of the $CO_2 + H_2$ state corresponds to infinite separation (no lateral interactions included). Similarly, for the redox mechanism, the free energy barriers used in the plots correspond to CO_2 dissociation with no coadsorbed 2H, and the free energy barriers for the associative mechanism correspond to CO_2 + H reactions to COOH, m-HCOO and b-HCOO with no other coadsorbed H species. In this way, the free energy barriers of the different reaction pathways are more comparable.

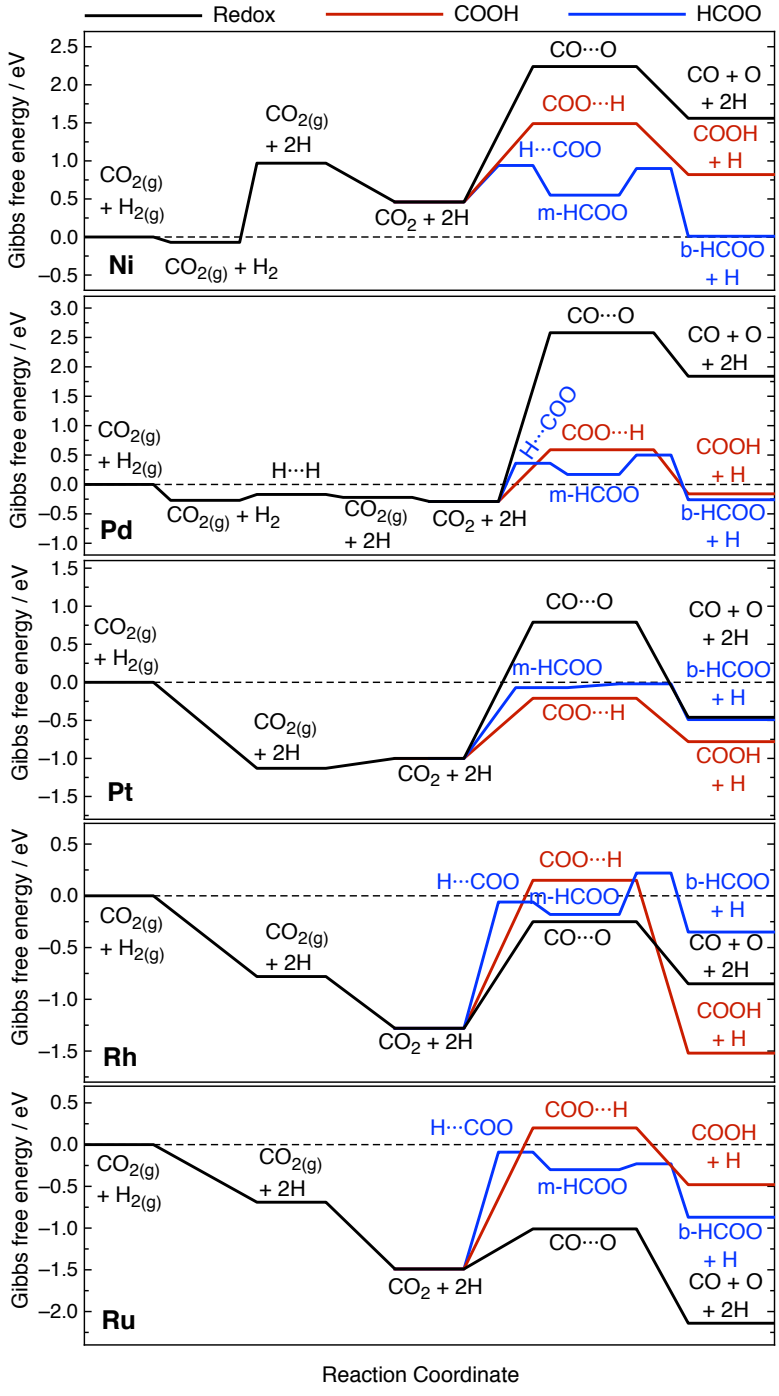

4. Conclusions

CO_2 adsorption and subsequent activation have been investigated by means of periodic DFT calculations for the full set of 3*d*, 4*d*, and 5*d* TM SACs supported on zeolite S-1, namely TM_1@S-1. The steps considered include adsorption and dissociation of CO_2 and H_2 species, as well as CO_2 reaction with adsorbed H to produce COOH or HCOO intermediates. The catalytic properties are mainly controlled by the encapsulated TM atoms, since CO_2 and H_2 interact very weakly with the S-1 framework structure. In general, CO_2 binds strongly to TM atoms and receives electron density from the TM, ending up being negatively charged. Those effects are particularly strong for those TMs in the bottom left of the periodic table and become less pronounced when moving right along a period or up in a group. On the other hand, H_2 chemisorbs on TMs from groups 3, 4, 5, 9, 10 and Os with negligible charge transfer from the TM. Noticeably, TMs from groups 11−12 hardly interact with CO_2 and H_2, where both species are physisorbed. TMs in groups 3−9 exhibit very low energy barriers for direct CO_2 dissociation, suggesting that CO_2 conversion reactions on these SACs would follow the redox mechanism. However, the COOH- or HCOO-mediated associative mechanism is more favoured in group 10 TMs, according to the free energy profiles. Finally, we predict group 11−12 TM SACs to have a very poor catalytic activity for CO_2 conversion, due to their weak interaction with CO_2 and H_2 as well as high energy barriers.

Combining the present results with the stability assessment of supported TM SACs in our previous contribution [43], we conclude that groups 3 and 10 TM SACs, as well as Rh_1@S-1 and Ru_1@S-1 are very promising candidates for CO_2 conversion reactions. All these catalysts exhibit low energy barriers and are predicted to have a strong resistance to aggregation/sintering due to their strong interactions with the zeolite wall. These results are in agreement with experimental observations stating that Ru and Rh were encapsulated in S-1 and used in different catalytic processes [39,40] with good stability and superior catalytic activity. With this contribution, we hope to narrow down the materials space for novel CO_2 conversion SACs and provide a solid theoretical background from which observed experimental features can be interpreted, understood, and discussed.

CrediT authorship contribution statement

Gerard Alonso: Conceptualization, Methodology, Formal analysis, Investigation, Writing – original draft, Writing – review & editing. **Hector Prats:** Conceptualization, Methodology, Formal analysis, Writing – review & editing. **Estefanía López:** Methodology, Investigation, Writing – review & editing. **Fermín Huarte-Larrañaga:** Methodology, Investigation, Writing – review & editing. **Ramón Sayós:** Project administration, Funding acquisition, Writing – review & editing. **Pablo Gamallo**: Supervision, Methodology, Investigation, Funding acquisition, Writing- review & editing.

Declaration of competing interest

The authors declare that they have no known competing financial interests or personal relationships that could have appeared to influence the work reported in this paper.

Acknowledgments

Support to this research is granted by the Spanish Ministry of Science, Innovation and Universities (Grants RTI2018-094757-B-I00, MCIU/AEI/FEDER, UE and MDM-2017-0767) and by the Generalitat de Catalunya (Grant 2017SGR0013 and P.G. Serra Hunter Associate Professorship). Authors thank to the Red Española de Supercomputación (RES) for the supercomputing time granted (QS-2021-1-0035 and QS-2020-3-0023).

Appendix A. Supplementary data

Supplementary material related to this article can be found online at (to be filled by the editorial).

Also, all optimized VASP CONTCAR geometry files for those snapshots are supplied on a public Github repository: https://github.com/Gerard-Alonso/Zeolite-encapsulated-single-atom-catalysts-for-efficient-CO2-conversion

References

[1] C.P. Morice, J.J. Kennedy, N.A. Rayner P.D. Jones, Quantifying uncertainties in global and regional temperature change using an ensemble of observational estimates: The HadCRUT4 data set. J. Geophys. Res-Atmos. 117 (2012) D08101:1-22.

[2] K. Jalama, Carbon dioxide hydrogenation over nickel-, ruthenium-, and copper-based catalysts: Review of kinetics and mechanism. Catal. Rev. 59 (2017) 95-164.

[3] S. Kattel, P. Liu, J.G. Chen, Tuning selectivity of CO_2 hydrogenation reactions at the metal/oxide interface. J. Am. Chem. Soc. 139 (2017) 9739-9754.

[4] W. Li, H. Wang, X. Jiang, J. Zhu, Z. Liu, X. Guo, C. Song, A short review of recent advances in CO_2 hydrogenation to hydrocarbons over heterogeneous catalysts. RSC Adv. 8 (2018) 7651-7669.

[5] W. Wang, S. Wang, X. Ma, J. Gong, Recent advances in catalytic hydrogenation of carbon dioxide. Chem. Soc. Rev. 40 (2011) 3703-3727.

[6] X. Nie, W. Li, X. Jiang, X. Guo, C. Song, Recent advances in catalytic CO_2 hydrogenation to aclohols and hydrocarbons. Adv. Catal. 65 (2019) 121-133.

[7] A. Morales-García, F. Viñes, J. R. B.Gomes, F. Illas, Concepts, models, and methods in computational heterogeneous catalysis illustrated through CO_2 conversion. WIREs Comput. Mol. Sci. 11 (2021) e1530.

[8] Y. Hartadi, D. Widmann, R.J. Behm, CO_2 hydrogenation to methanol on supported Au catalysts under moderate reaction conditions: support and particle size effects. ChemSusChem. 8 (2015) 456-465.

[9] J. Qu, X. Zhou, F. Xu, X.Q. Gong, S.C.E. Tsang, Shape effect of Pd-promoted Ga_2O_3 nanocatalysts for methanol synthesis by CO_2 hydrogenation. J. Phys. Chem. C 118 (2014) 24452-24466.

[10] S. Kuld, M. Thorhauge, H. Falsig, C.F. Elkjær, S. Helveg, I. Chorkendorff; J. Sehested, Quantifying the promotion of Cu catalysts by ZnO for methanol synthesis. Science 352 (2016) 969-974.

[11] K.P Yu, W.Y. Yu, M.C. Kuo, Y.C. Liou, S.H. Chien, Pt/titania-nanotube: A potential catalyst for CO_2 adsorption and hydrogenation. Appl. Catal. B-Environ. 84 (2008) 112-118.

[12] L. Falbo, M. Martinelli, C.G. Visconti, L. Lietti, C. Bassano, P. Deiana, Kinetics of CO_2 methanation on a Ru-based catalyst at process conditions relevant for power-to-gas applications. App. Catal. B-Environ. 225 (2018) 354-363.

[13] J.N. Park, E.W. McFarland, A highly dispersed Pd-Mg/SiO_2 catalyst active for methanation of CO_2. J. Catal. 226 (2009) 92-97.

[14] F.W. Chang, M.S. Kuo, M.T. Tsay, M.C. Hsieh, Hydrogenation of CO_2 over nickel catalysts on rice husk ash-alumina prepared by incipient wetness impregnation. App. Catal. A-Gen. 247 (2003) 309-320.

[15] A. Wang, J. Li and T. Zhang, Heterogeneous single-atom catalysis. Nat. Rev. Chem. 2 (2018) 65-81.

[16] T. Zhu, Y. Han, S. Liu, B. Yuan, Y. Liu, H. Ma. Porous materials confining single atoms for catalysis. Front. Chem. 9 (2021) 717201:1-11.

[17] H. Zhang, L. Guigao, L. Shi, J. Ye, Single-atom catalysts: Emerging multifunctional materials in heterogeneous catalysis. Adv. Energy Matter. 8 (2018) 1701343:1-24.

[18] S.K. Kaiser, Z. Chen, D.F. Akl, S. Mitchell, J. Pérez-Ramírez, Single-atom catalysts across the periodic table. Chem. Rev. 120 (2020) 11703-11809.

[19] B. Qiao, A. Wang, X. Yang, L.F. Allard, Z. Jiang, Y. Cui, J. Liu, J. Li, Zhang, T. Single-atom catalysisof CO oxidation using Pt_1/FeO_x. Nat. Chem. 3 (2011) 634-641.

[20] M. Yang, L.F. Allard, M. Flytzani-Stephanopoulos, Atomically dispersed Au-(OH)x species bound on titania catalyze the low-temperature water-gas shift reaction. J. Am. Chem. Soc. 135 (2013) 3768-3771.

[21] J. Lin, A. Wang, B. Qiao, X. Liu, X. Yang, X. Wang, J. Liang, J. Li, J. Liu, T. Zhang, Remarkable performance of Ir_1/FeO_x single-atom catalyst in water gas shift reaction. J. Am. Chem. Soc. 135 (2013) 15314-15317.

[22] R. Lang, T. Li, D. Matsumura, S. Miao, Y. Ren, Y.T. Cui, Y. Tan, B. Qiao, L. Li, A. Wang, X. Wang, T. Zhang, Hydroformylation of olefins by a rhodium single-atom catalyst with activity comparable to $RhCl(PPh_3)_3$. Angew. Chem. Int. Ed. 55 (2016) 16054-16058.

[23] S. Sun, G. Zhang, N. Gauquelin, N. Chen, J. Zhou, S. Yang, W. Chen, X. Meng, D. Geng, M.N. Banis, R. Li, S. Ye, S. Knights, G.A. Botton, T.K. Sham, X. Sun, Single-atom catalysis using Pt/Graphene achieved through atomic layer deposition. Sci. Rep. 3 (2013) 1775:1-9.

[24] D. Deng, X. Chen, L. Yu, X. Wu, Q. Liu, Y. Liu, H. Yang, H. Tian, Y. Hu, P. Du, R. Si, J. Wang, X. Cui, H. Li, J. Xiao, T. Xu, J. Deng, F. Yang, P.N. Duchesne, P. Zhang, J. Zhou, L. Sun, J. Li, X. Pan, X. Bao, A single iron site confined in a graphene matrix for the catalytic oxidation of benzene at room temperature. Sci. Adv. 1 (2015) e1500462:1-9.

[25] P. Liu, Y. Zhao, R. Qin, S. Mo, G. Chen, L. Gu, D.M. Chevrier, P. Zhang, Q. Guo, D. Zhang, B. Wu, G. Fu, N. Zheng, Photochemical route for synthesizing atomically dispersed palladium catalysts. Science 13 (2016) 797-800.

[26] X.Q. Gong, A. Selloni, O. Dulub, P. Jacobson, U. Diebold, Small Au and Pt clusters at the anatase TiO_2(101) surface: Behavior at terraces, steps and surface oxygen vacancies. J. Am. Chem. Soc. 130 (2008) 370-381.

[27] A.W. Robertson, B. Montanari, K. He, J. Kim, C.S. Allen, Y.A. Wu, J. Olivier, J. Neethling, N. Harrison, A.I. Kirkland, J.H. Warner, Dynamics of single Fe atoms in graphene vacancies. Nano Lett. 13 (2013) 1468-1475.

[28] H. Wang, Q. Wang, Y. Chen, K. Li, Y. Yao, Q. Zhang, C. Dong, P. Wang, U. Schwingenschlögl, W. Yang, X.X. Zhang, Doping monolayer graphene with single atom substitutions. Nano Lett. 12 (2012) 141-144.

[29] J.O. Ehresmann, P.W. Kletnieks, A. Liang, V.A. Bhirud, O.P. Bagatchenko, E.J. Lee, M. Klaric, B.C. Gates, J.F. Haw, Evidence from NMR and EXAFS studies of a dynamically uniform mononuclear single-site zeolite supported rhodium catalyst. Angew. Chem. Int. Ed. 45 (2006) 574-576.

[30] Y. Chen, S. Ji, C. Chen, Q. Peng, D. Wang, Y. Li, Synthetic strategies and electrochemical applications. Joule 2 (2018) 1242-1264.

[31] L. Liu, A. Corma, Confining isolated atoms and clusters in crystalline porous materials for catalysis. Nat. Rev. Mater. (2020) 1-20.

[32] X. Dong, X. Liu, Y. Chen, M. Zhang, Screening of bimetallic M-Cu-BTC MOFs for CO_2 activation and mechanistic study of CO_2 hydrogenation to formic acid: A DFT study. J. CO2 Util. 24 (2018) 64-72.

[33] H. Wang, L. Wang, F. Xiao, Metal@zeolite hybrid materials for catalysis. ACS Cent. Sci. 6 (2020) 1685-1697.

[34] J.D. Kistler, X. Chotigkrai, P. Xu, B. Enderle, P. Praserthdam, C.Y. Chen, N.D. Browning, B.C. Gates, A single-site platinum CO oxidation catalyst in zeolite KLTL: Microscopic and spectroscopic determination of the locations of the platinum atoms. Angew. Chem. Int. Ed. 53 (2014) 8904-8907.

[35] S. V. Konnov, F. Dubray, E.B. Clatworthy, C. Kouvatas, J. Gilson, J. Dath, D. Minoux, C. Aquino, V. Valtchev, S. Moldovan, S. Koneti, N. Nesterenko, S. Mintova. Novel strategy for the synthesis of ultra-stable single-site Mo-ZSM-5 zeolite nanocrystals. Angew. Chem. Int. Ed. 59 (2020) 19553-19560.

[36] J. Shan, M. Li, L.F. Allard, S. Lee, M. Flytzani-Stephanopoulos, Mild oxidation of methane to methanol or acetic acid on supported isolated rhodium catalysts. Nature 551 (2017) 605-608.

[37] Y. Liu, Z. Li, Q. Yu, Y. Chen, Z. Chai, G. Zhao, S. Liu, W.C. Cheong, Y. Pan, Q. Zhang, L. Gu, L. Zheng, Y. Wang, Y. Lu, D. Wang, C. Chen, Q. Peng, Y. Liu, L. Liu, J. Chen, Y. Li, A general strategy for fabricating isolated single metal atomic site catalysts in Y zeolite. J. Am. Chem. Soc. 141 (2019) 9305-9311.

[38] Z. Li, Q. Ren, X. Wang, W. Chen, L. Leng, M. Zhang, J. H. Horton, B. Liu, Q. Xu, W. Wu, J. Wang. Highly active and stable palladium single-atom catalyst achieved by a thermal atomization strategy on an SBA-15 molecular sieve for semi-hydrogenation reactions. ACS Appl. Mater. Interfaces. 13 (2021) 2530-2537.

[39] Q. Sun, N. Wang, T. Zhang, R. Bai, A. Mayoral, P. Zhang, Q. Zhang, O. Terasaki, J. Yu, Zeolite-encaged single-atom rhodium catalysts: Highly-efficient hydrogen generation and shape-selective tandem hydrogenation of nitroarenes. Angew. Chem. Ind. Ed. 58 (2019) 18570-18576.

[40] J.Z. Qiu, J. Hu, J. Lan, L.F. Wang, G. Fu, R. Ziao, B. Ge, J. Jiang, Pure siliceous zeolite-supported Ru single-atom active sites for ammonia synthesis. Chem. Matter. 31 (2019) 9413-9421.

[41] A Corma, M.E. Davis, Issues in the synthesis of crystalline molecular sieves: towards the crystallization of low framework-density structures. ChemPhysChem 5 (2004) 304-313.

[42] Y. Chai, W. Shang, W. Li, G. Wu, W. Dai, N. Guan, L. Li, Noble metal particles confined in zeolites: synthesis, characterization, and applications. Adv. Sci. 6 (2019) 1900299:1-19.

[43] H. Prats, G. Alonso, R. Sayós, P. Gamallo, Transition metal atoms encapsulated within microporous silicalite-1 zeolite: A systematic computational study. Micropor. Mesopor. Mat. 308 (2020) 110462:1-8.

[44] G. Kresse, J. Furthmüller, Efficient iterative schemes for ab initio total-energy calculations using a plane-wave basis set. Phys. Rev. B. 54 (1996) 11169-11186.

[45] J.P. Perdew, K. Burke, M. Ernzerhof, Generalized gradient approximation made simple. Phys. Rev. Lett. 77 (1996) 3865-3868.

[46] S. Grimme, J. Anthony, S. Ehrlich, S. Krieg, A consistent and accurate ab initio parametrization of density functional dispersion correction (DFT-D) for the 94 elements H-Pu. J. Chem. Phys. 132 (2010) 154104:1-19.

[47] P.E. Blöch, Projector augmented-wave method. Phys. Rev. B: Condens. Matter. Phys. 50 (1994) 17953-17979.

[48] G. Kresse, D. Joubert, From ultrasoft pseudopotentials to the projector augmented-wave method. Phys. Rev. B: Condens. Matter. Phys. 59 (1999) 1758-1775.

[49] G. Henkelman, B.P. Uberuaga, H. Jónsson, A climbing image nudged elastic band method for finding saddle points and minimum energy paths, J. Chem. Phys. 113 (2000) 9901–9904.

[50] S. Smidstrup, A. Pedersen, K. Stokbroand, H. Jónsson, Improved initial guess for minimum energy path calculations. J. Chem. Phys. 140 (2014) 214106:1-6.

[51] A.H. Larsen, J.J. Mortensen, J. Blomqvist, I.E. Castelli, R. Christensen, M. Dułak, J. Friis, M.N. Groves, B. Hammer, C. Hargus, E.D. Hermes, P.C. Jennings, P. Bjerre Jensen, J. Kermode, J.R. Kitchin, E. Leonhard Kolsbjerg, J. Kubal, K. Kaasbjerg, S. Lysgaard, J. Bergmann Maronsson, T. Maxson, R. Olsen, L. Pastewka, A. Peterson, C. Rostgaard, J. Schiøtz, O. Schütt, M. Strange, K.S. Thygesen, T. Vegge, L. Vilhelmsen, M. Walter, Z. Zeng, K.W. Jacobsen, The atomic simulation environment—a python library for working with atoms. J. Phys.: Condens. Matter. 29 (2017) 273002:1-31.

[52] D. A. McQuarrie. Statistical Mechanics, University science books: Sausalito, 2013.

[53] R. F. W. Bader, A Quantum Theory of Molecular Structure and its Applications. Chem. Rev. 91 (1991) 893–928.

[54] K. Werner, X. Weng, F. Calaza, M. Sterrer, T. Kropp, J.Paier, J. Sauer, M. Wilde, K. Fukutani, S. Shaikhutdinov, H.J., Freund. Towards and Understanding of Selective Alkyne Hydrogenation on Ceria: On the Impact of O Vacancies on H2 Interaction with CeO_2(111). J. Am. Chem. Soc. 139 (2017) 17608-17616.

[55] W. Zhang, M. Pu, M. Lei. Theoretical Studies on the Stability and Reactivity of the Metal-Doped CeO_2 (100) Surface: Toward H_2 Dissociation and Oxygen Vacancy Formation. Langmuir 36 (2020) 5891-5901.

[56] Y. Liu, Q. Wang, H. Liu, K. Li, L. Jia, D. Li, B. Hou, B. Wang. Insights into the Metal-Support Interaction Between

NiCu Cluster and MgO as well as its Effect on H Adsorption and H_2 Dissociation. Molec. Catal. 436 (2017) 111-119.

[57] H. Prats, J.J. Piñeiro, F. Viñes, S.T. Bromley, R. Sayós, F. Illas. Assessing the usefulness of transition metal carbides for hydrogen reactions. Chem. Commun. 55 (2019) 12797.

[58] W. Li, H. Wang, X. Jiang, J. Zhu, Z. Liu, X. Guo, C. Song, A short review of recent advances in CO_2 hydrogenation to hydrocarbons over heterogeneous catalysts. RSC Adv. 8 (2018) 7651-7669.

[59] M. Zhang, B. Zijlstra, I.A.W. Filot, F. Li, H. Wang, J. Li, E.J.M. Hensen, A theoretical study of the reverse water-gas shift reaction on Ni(111) and Ni(311) surfaces. Can. J. Chem. Eng. 98 (2020) 740-748.

[60] L. Dietz, S. Piccinin, M. Maestri, Mechanistic insights into CO_2 activation via reverse water-gas shift on metal surfaces. J. Phys. Chem. C. 119 (2015) 4959-4966.

[61] P. Lozano-Reis, H. Prats, P. Gamallo, F. Illas, R. Sayós, Multiscale study of the mechanism of catalytic CO_2 hydrogenation: role of the Ni(111) facets. ACS Catal. 10 (2020) 8077-8089.

[62] J. Niu, J. Ran, W. Qi, Z. Ou, W. He, Identification of active sites in CO_2 activation on MgO supported Ni cluster. Int. J. Hydrogen. Energ. 45 (2020) 11108-11115.

[63] P. Schlexer, H.Y. Tiffany-Chen, G. Pacchioni, CO_2 activation and hydrogenation: a comparative DFT study of Ru_{10}/TiO_2 and Cu_{10}/TiO_2 model catalysts. Catal. Lett. 147 (2017) 1871-1881.

[64] H. Jing, Q. Li, J. Wang, D. Liu, K. Wu, Theoretical study of the reverse water gas shift reaction on copper modified β-Mo2C(001) surface. J. Phys. Chem. C. 123 (2019) 1235-1251.

[65] V. Pallassana, M. Neurock, Electronic Factors Governing Ethylene Hydrogenation and Dehydrogenation Activity of Pseudomorphic PdML/Re(0001), PdML/Ru(0001), Pd(111), and PdML/Au(111) Surfaces. J. Catal. 191 (2000) 301-317.

[66] J.K. Nørskov, F. Studt, F. Abild-Pedersen, T. Bligaard, Fundamental concepts in heterogeneous catalysis, John Wiley & Sons, Inc.: Hoboken, 2014.

[67] J.N. Brønsted, Acid and Basic Catalysis. Chem. Rev. 5 (1928) 231–338.

[68] M.G. Evans, M. Polanyi, Inertia and Driving Force of Chemical Reactions. Trans. Faraday Soc. 34 (1938) 11–24.

[69] S. Wang, B. Temel, J. Shen, G. Jones, L.C. Grabow, F. Studt, T. Bligaard, F. Abild-Pedersen, C.H. Christensen, J.K. Nørskov, Universal Brønsted-Evans-Polanyi relations for C-C, C-O, C-N, N-O, N-N, and N-O dissociation reactions. Catal. Lett. 141 (2011) 370-373.

[70] J. F. Costa-Serra, C. Cerdá-Moreno, A. Chica. Zeolite-supported Ni catalysts for CO_2 methanation: effect of zeolite structure and Si/Al ratio. Appl. Sci. 10 (2020) 5131:1-14.

[71] H. Prats, L. Álvarez, F. Illas, R. Sayós. Kinetic Monte Carlo simulations of the water gas shift reaction on Cu(111) from density functional theory based calculations. J. Catal. 333 (2016) 217-226.